Plasmonic analog of electromagnetically induced absorption: simulations, experiments, and coupled oscillator analysis

Richard Taubert,[1] Mario Hentschel,[1,2] and Harald Giessen[1,*]

[1]*4th Physics Institute and Research Center SCoPE, University of Stuttgart, D-70569 Stuttgart, Germany*
[2]*Max Planck Institute for Solid State Research, Heisenbergstrasse 1, D-70569 Stuttgart, Germany*
**Corresponding author: giessen@physik.uni-stuttgart.de*

Received September 5, 2013; revised October 3, 2013; accepted October 5, 2013;
posted October 8, 2013 (Doc. ID 196997); published November 5, 2013

We present a comprehensive analysis of the plasmonic analog of electromagnetically induced absorption. Interaction of plasmonic dipoles with plasmonic quadrupoles in the special case for nonvanishing retardation introduces an additional phase factor in the coupling constant, which can result in constructive interference of the two resonances. This leads to narrow resonances in the complex plasmonic absorption spectrum. We present simulations for a broad parameter space, matching experiments, as well as an extensive model analysis. Our paper comprises a situation that represents an intermediate plasmonic coupling regime, between near-field and far-field coupling.

OCIS codes: (160.1245) Artificially engineered materials; (160.4236) Nanomaterials.
http://dx.doi.org/10.1364/JOSAB.30.003123

1. INTRODUCTION

Up to now, plasmonic coupling has been regarded mostly in the limiting cases of either purely quasi-static near-field or purely radiative far-field interaction. Here, we discuss the interesting situation of plasmonic coupling in the intermediate regime between near and far field. Near-field interaction is characterized by the complete absence of radiative or wave effects, i.e., propagation phases are meaningless. By contrast, radiative interaction is solely described by far-field effects. It is assumed that the near fields of the oscillators have decayed sufficiently to not mediate any interaction and therefore, their complete absence is assumed.

In this paper, we discuss a structure in which both, near- and far-field coupling effects, take place at the same time. A plasmonic dipole wire coupled to a quadrupolar wire pair exhibits features of radiative coupling such as phase retardation between oscillators, while at the same time excitation of the quadrupole oscillation is possible, which is a near-field effect.

This introduces the ability to manipulate the phase shift between two-coupled plasmonic resonances in a controlled fashion. We theoretically and experimentally demonstrate that in the intermediate regime, the coupling of a broad dipolar to a narrow, dark quadrupolar plasmon resonance is possible while simultaneously allowing a retardation-induced phase shift. The additional phase will be used to tune the interaction phase of the oscillators and change the destructive interference that is present in the plasmonic analog of electromagnetically induced transparency (EIT) [1] to constructive interference and hence, increased absorption. This system exhibits similarities to the atomic physics effect of electromagnetically induced absorption (EIA) and thus will be termed the classical analog of EIA.

First, a short review of EIT in atomic and classical systems is given; then the plasmonic analog of EIT will be discussed, followed by the presentation of the classical plasmonic analog of EIA [2–4].

2. EIT AND EIA IN ATOMIC SYSTEMS

EIT is an inherently quantum mechanical effect, which occurs in specifically prepared atomic three-level systems [5]. It was first proposed and experimentally realized by Harris and coworkers [6,7]. Usually, a Λ configuration as depicted in Fig. 1 is used. Energy level $|1\rangle$ is coupled to the ground state $|0\rangle$ by a bright dipole-allowed transition with resonance frequency ω_0. At the same time, it is coupled to a dark state $|2\rangle$, which might be detuned by a shift δ. The coupling is mediated by an additional coupling field provided by an additional laser, which ensures the coherence of both levels. The direct excitation $|0\rangle \rightarrow |2\rangle$ is dipole-forbidden; therefore, its decay rate γ_2 is smaller than the bright transition rate γ_1. However, the coupling of levels $|1\rangle$ and $|2\rangle$, described by the coupling parameter $\kappa \exp(i\varphi)$, allows a population of state $|2\rangle$, which will cause a back-action and an excitation of level $|1\rangle$. Overall, this level scheme allows two different excitation pathways leading to an occupation of the dipole-allowed state $|1\rangle$: the direct transition $|0\rangle \rightarrow |1\rangle$ and the indirect transition $|0\rangle \rightarrow |1\rangle \rightarrow |2\rangle \rightarrow |1\rangle$.

If the interference between these both pathways is destructive, the excitation $|0\rangle \rightarrow |1\rangle$ is not possible, light will not be absorbed, and a narrow transmission peak opens up. As the coupling between levels $|1\rangle$ and $|2\rangle$ and thus the possibility of interference is mediated by the coupling laser field, the effect is termed EIT.

EIT can be considered as a special case of a Fano resonance [8]. Whereas the general Fano resonance formula describes a

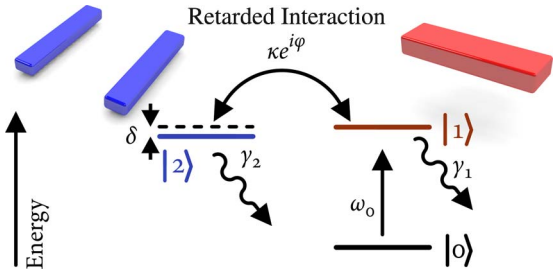

Fig. 1. Three-level model scheme for the coupled plasmonic dipole–quadrupole system. Energy level $|1\rangle$ can be excited from the ground level $|0\rangle$ by a bright transition with a large dipole moment and is simultaneously coupled to a dark state $|2\rangle$. In a usual EIT system, the coupling parameter κ is real. If it is possible to apply an additional phase factor $e^{i\varphi}$, e.g., by using a retarded coupling mechanism, the type of interference between both pathways can be changed from destructive to constructive, resulting in either EIT or EIA.

multitude of phenomena, which can be explained by the interference of excitation pathways, and thus results in a variety of different asymmetric line shapes, EIT is a special case for perfect destructive interference of two excitation paths and yields the typical spectral shape of a narrow transmittance window imposed onto a broad dipolar transmittance line shape.

A complementary process to EIT would be the enhancement of absorption in an atomic system by a coherent effect. In atomic physics, this has been realized using degenerate two-level systems and has been termed EIA [9–12]. In this case, two branches of the degenerate ground state form the two lower levels of the Λ system. When driving the system with a coupling laser, a narrow, sublinewidth peak of enhanced absorbance is observed on top of the broader dipolar absorbance peak.

3. EIT IN CLASSICAL SYSTEMS AND PLASMONICS

Even though EIT is a quantum mechanical effect involving interference of probability amplitudes, EIT-like effects can be observed in classical systems such as plasmas [13,14] and even in very fundamental systems such as coupled mechanical oscillators and L-C-resonators [15,16]. The realization of EIT in classical optical systems is of particular interest. There it emerges from the interference of the normal modes rather than from the quantum interference of excitation probabilities. This was first realized using evanescently coupled high-Q microresonators [17–22], and recently, in metamaterials [23–25] and plasmonic structures [1,26–35]. An effect similar to EIT and EIA is the so-called superscattering, where the higher modes of a structure are tuned such that their scattering amplitudes overlap with their fundamental dipolar mode and therefore, contribute substantially to the total scattering of the particle. This leads to a narrow scattering peak on top of the broad dipolar scattering resonance. However, this has been predicted only theoretically up to now [3,36,37].

Besides the physical peculiarity of the EIT effect itself, there are numerous applications, which make it very useful and therefore, a realization in systems other than cold atomic gases would be very convenient. For example, EIT can be harnessed to enhance nonlinear interaction in optical media [5], for dispersion engineering, in particular, the realization of slow light [17,20,22] or delay lines [22,25], reduction of losses [24], or plasmonic sensing with narrow linewidths [26,31].

In a classical system, EIT is realized by substituting bright and dark transitions for oscillators with different damping constants. Particularly, in a plasmonic system, the transitions are represented by metallic cut-wires: a quadrupolar cut-wire pair, which exhibits no net dipole moment and therefore, does not couple to the far field, is used for the dark transition and a dipolar cut-wire is used for the bright transition. A schematic of the stacked structure is depicted in Fig. 2, where the relevant dimensions are also introduced. In contrast to EIT in atomic physics, where a probe laser is used to monitor the spectral response of the system, the effect can be directly observed by acquiring white light spectra of the structure with light polarized parallel to the dipolar wire. Furthermore, the coupling between both oscillators is not mediated by the use of a coupling laser, but rather by the plasmonic near fields of the oscillators themselves. Hence, it is favorable to maximize the (near-field) coupling strength between the quadrupole and the dipole. In contrast to a planar side-by-side arrangement, a stacked arrangement exhibits a substantially higher coupling strength and therefore, an increased modulation depth for the effect [1]. The coupling strength can be tuned by varying the offset parameter S. For $S = 0$ nm, no coupling between the dipole and the quadrupole is possible due to symmetry considerations. For increasing offset, an excitation of the quadrupole via the near field of the dipole is possible. Therefore, the near-field coupling strength, represented by S, is analogous to the coupling laser field strength Ω_c in atomic systems.

4. MODES OF THE EIT STRUCTURE

Electromagnetic field calculations are used to investigate the basic principles of the structure. These are performed using a Finite Integration Technique solver, which is commercially

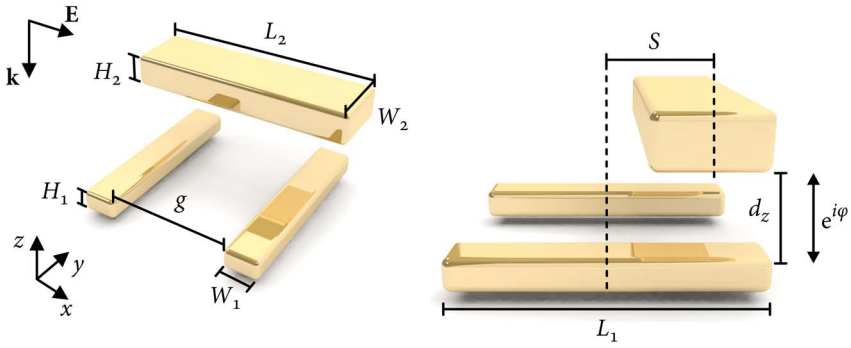

Fig. 2. Geometry parameters of the structure. The phase difference between the dipole and the quadrupole can be tuned by changing the vertical spacing d_z.

available (CST Microwave Studio). We assume the dielectric materials to be dispersion-free; the gold is modeled as a Drude metal with a plasma frequency of $\omega_p = 2073$ THz and a damping parameter of $\gamma_D = 20$ THz. Figure 3 displays a set of field calculations for different frequencies of incoming light, namely, at both transmittance dips (at 150 and 201 THz) and at the EIT peak (176 THz). The z component of the electric field in planes slightly above the corresponding oscillators is displayed. This field component corresponds to the normal field on the respective surface, which is tightly connected to the charge distribution and therefore, the plasmon oscillation within the wires. As structural parameters, the values of Liu *et al.* [1], $L_1 = 315$ nm, $L_2 = 355$ nm, $H_1 = H_2 = 40$ nm, $W_1 = W_2 = 80$ nm, $d_z = 30$ nm, $g = 220$ nm, and $S = 120$ nm, are used. Periodicity is 700 nm in both directions.

Figure 3(a) shows the calculated transmittance spectrum, which exhibits the characteristic shape of a window of high transmittance on top of the broader dipolar transmittance dip. Figures 3(b)–3(d) show the amplitude of the electric field z component on a plane slightly above the dipole and the quadrupole. Temporally, the fields are displayed at the point of maximum field intensity. For the points of minimum transmittance, i.e., at frequencies of 150 THz [Fig. 3(b)] and 201 THz [Fig. 3(d)], one can observe two of the expected modes [38,39] in a coupled three-particle system: both quadrupole wires oscillate exactly antipodal due to the symmetry and excitation mechanism. Therefore, they exhibit a typical quadrupolar charge distribution, which cancels in the far field and hence, this mode cannot couple to far-field radiation on its own.

The polarization of the dipole wire takes two orientations with respect to the quadrupole: in case of Fig. 3(b), the quadrupolar and dipolar wire ends, which are faced toward each other, exhibit opposite charges, analogous to the antisymmetric mode in the wire pairs. Therefore, this mode will be referred to as the antisymmetric mode of the structure. Electrostatic energy is decreased, and therefore, this mode is red-shifted from the single oscillator resonance positions. In case of Fig. 3(d), the nanowire ends facing each other exhibit equal charges, which resembles the symmetric mode of a wire pair; thus, the resonance position is blue-shifted and the mode will be referred to as the symmetric mode. Between these modes, namely, at the transmittance peak, almost no field intensity is observed at the dipole and only the quadrupole wires exhibit a plasmonic oscillation. This is depicted in the field plot for a frequency of 176 THz. It is possible to interpret this in terms of a destructive interference of the two modes. In this picture, the cancellation of the dipole wire plasmon oscillation is a direct analog to the inhibited population of state $|1\rangle$ due to the destructive interference of probability amplitudes; thus, the effect can indeed be termed the classical analog of EIT.

5. PHASE TUNING AND THE TRANSITION TO EIA

To realize EIA it is necessary to change the destructive interference to a constructive interference. In an atomic system, special care has to be taken in order to achieve this. However, the realization for classical oscillators appears quite straightforward: one can simply tune the oscillator phases in order to change the type of interference between them. While this again is a quite challenging task for mechanical oscillators connected by springs, in an optical system retardation is present and can be harnessed for phase tuning by increasing the vertical distance of the building blocks.

The behavior of the system will be examined by calculating the spectra for different vertical distances d_z between the dipole and the quadrupole. Figure 4(a) shows the calculated transmittance, reflectance, and absorbance of the structure for the dimensions stated above. The offset is $S = 120$ nm, which corresponds to maximum coupling strength between the dipole and the quadrupole. To display the pure effect undisturbed by nonradiative damping due to ohmic losses in the metal, the damping parameter in the Drude model for gold has been reduced to $\gamma_D = 1$ THz.

For small d_z, the transmittance graph shows the typical behavior of the EIT structure with a narrow transmittance peak imposed onto the dipolar transmittance dip. Remarkably, for

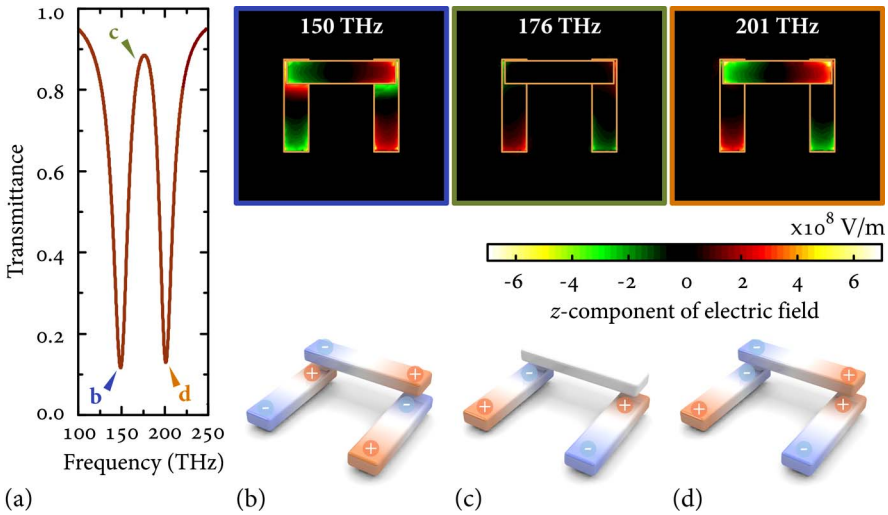

Fig. 3. (a) Calculated transmittance spectrum of the EIT structure, with arrowheads indicating the spectral positions at which electric field calculations (b)–(d) were performed. (b)–(d) Calculated z component of the electric field for the EIT structure with $d_z = 30$ nm for different spectral positions, (b) 150 THz, (c) 176 THz, and (d) 201 THz. At the transmittance minima, a characteristic (b) antisymmetric and (d) symmetric field distribution is observed. Interference between these two modes of the structure leads to the cancellation of dipole oscillation in the case of (c) and hence, the observation of the EIT peak. The bottom row shows a schematic of the charge distribution for the different situations.

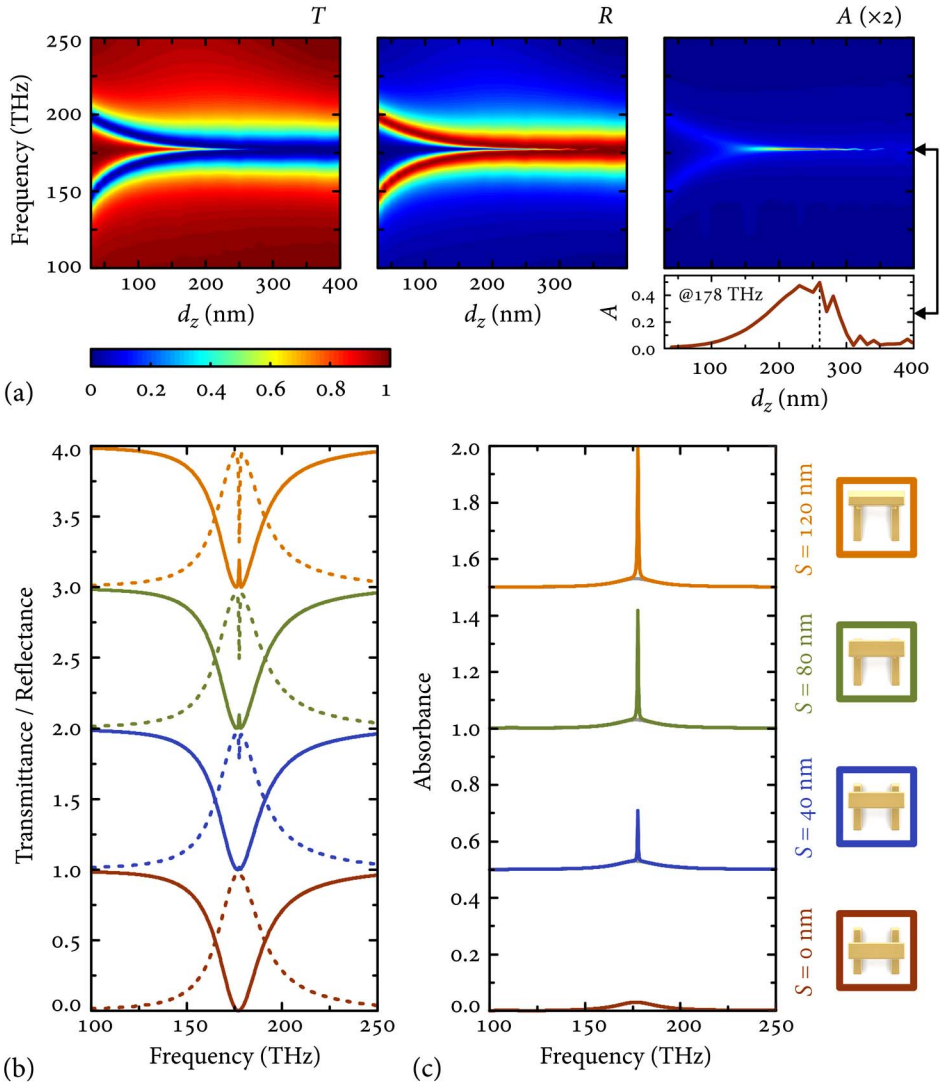

Fig. 4. (a) Color-coded calculated transmittance, reflectance, and absorbance spectra for increasing vertical spacing d_z between the dipole and the quadrupole and maximum coupling strength. (b) Calculated transmittance (solid curve) and reflectance (dashed curve) and (c) absorbance for the EIA structure with increasing offset of $S = 0$–120 nm and a vertical spacing of $d_z = 260$ nm. To show the effect unhampered by nonradiative damping, the damping coefficient in the Drude model is set to $\gamma_D = 1$ THz in this calculation.

very small distances the spectra look similar to a conventional near-field splitting in a dimer structure. The increasing spectral splitting for these very small distances stems from the increased coupling strength and is also present in atomic systems where it is termed Autler–Townes splitting [40,41].

On increasing vertical spacing, the near-field coupling strength is decreased and the spectra resemble a case of badly tuned EIT, as the modulation of the transmittance peak becomes smaller. However, a pronounced difference in transmittance and reflectance can be observed: the modulation of the dip in reflectance is much stronger than that of the peak in transmittance, indicating there is a change in *absorbance*. This can be seen in the absorbance spectra in the right panel, which are calculated via $A = 1 - T - R$. At the quadrupole resonance position, a very strong and narrow peak of increased absorbance is observed. This effect is largest for a vertical spacing of approximately $d_z = 260$ nm, as can be seen from the cross section plot below the absorbance graph. The retardation phase at this point is matched to obtain constructive interference and the absorbance is increased due to the coupling between the dipole and the quadrupole.

For this vertical distance, the calculated transmittance and reflectance for varying offset S and thus coupling strength are displayed in Fig. 4(b). The resulting absorbance is shown in Fig. 4(c). In case of symmetric arrangement ($S = 0$ nm, bottom row), coupling between the dipole and the quadrupole is not possible and only the dipolar absorbance is observed. As ohmic losses have been reduced artificially, the absorbance is rather low, with a maximum peak height of only 3%. By increasing the offset of the dipole, the coupling strength increases and a sharp absorbance feature at the quadrupole resonance position emerges on top of the dipole peak. This yields a double-peaked line shape. At this peak, the absorbance is substantially enhanced to an absolute value of 49%, which corresponds to an enhancement of more than one order of magnitude.

The spectra in Fig. 4(c) correspond very well to those observed in atomic EIA systems [9–11], with a very narrow peak that is substantially increased in height, compared with the

pure dipolar absorbance. To transfer this concept to plasmonics, however, it is important to note that ohmic losses in the plasmonic system constitute an additional loss mechanism, which is not present in atomic systems. This loss imposes a lower limit for the achievable linewidth in a plasmonic system and therefore, the appearance of the spectra changes substantially. Still, the underlying mechanism is valid for high damping values as well. Figure 5 shows calculations analogous to Fig. 4 with a realistic damping parameter, $\gamma_D = 20$ THz. The spectra show two distinct differences with respect to the idealized calculations of Fig. 4: first, the overall dipolar absorption is increased strongly. Whereas in the former case the pure dipolar absorption was 3%, it is now around 34%. As the maximum absorbance in the coupled case is not altered substantially and is still around 50%, the allover change in absorption strength is less dramatic. Second, the linewidth changes strongly. The low damping spectra exhibit a clear double-peaked shape due to the strong difference in linewidths ($\gamma_1/\gamma_2 \approx 30$), which cannot be observed easily for high damping. The reason is the additional nonradiative damping, which strongly broadens the quadrupolar resonance, leading to a ratio of only $\gamma_1/\gamma_2 \approx 2$.

6. EXPERIMENTAL REALIZATION

As discussed in the previous section, experimental observation of the EIA effect is hampered by spectral broadening due to nonradiative ohmic losses in the gold. Consequently, to improve the observability of the effect, it is desirable to reduce the bare dipolar absorbance compared with that of the quadrupolar mode. This is accomplished by changing the wire geometry: we increase the width W_2 and height H_2 of the dipole wire, preserving the spectral position by tuning the length L_2. Doing so leads to a relative change in the proportion of scattering and absorbance, as the optical response of small particles is dominated by absorption, whereas the response of larger particles is mostly determined by scattering. Similarly, the absorbance of the quadrupole can be increased

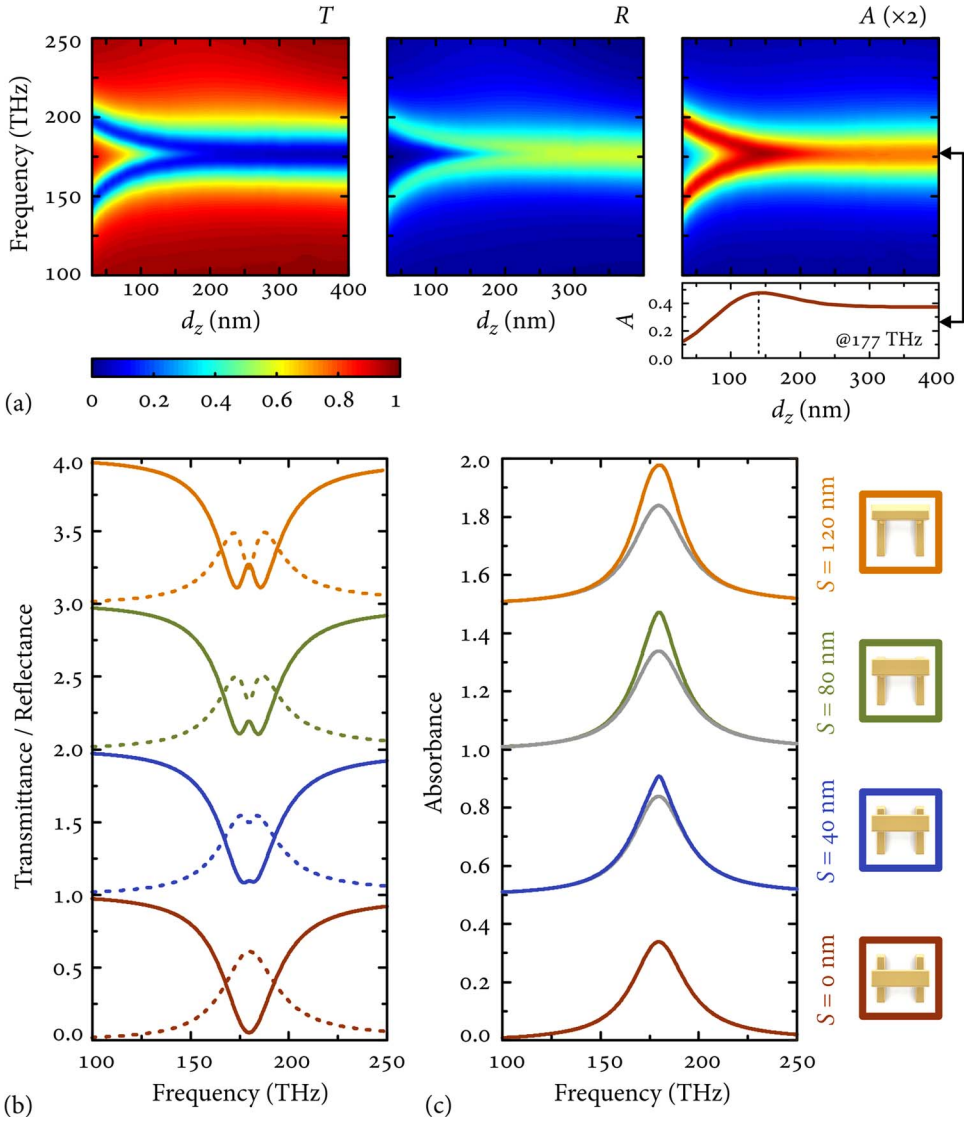

Fig. 5. (a) Color-coded calculated transmittance, reflectance, and absorbance spectra for increasing vertical spacing d_z between the dipole and the quadrupole and maximum coupling strength. (b) Calculated transmittance (solid curve) and reflectance (dashed curve) and (c) absorbance for the EIA structure with increasing offset of $S = 0$–120 nm and a vertical spacing of 140 nm. In this calculation, a realistic gold damping coefficient in the Drude model, $\gamma_D = 20$ THz, is assumed.

by reducing its wire cross section, still preserving the spectral position by tuning the length L_1. Additionally, a slight detuning δ of the spectral positions of the dipolar and quadrupolar mode is desirable, as this further facilitates the observation of the double-peaked line shape.

For this new, detuned geometry with quadrupole dimensions of $L_1 \times W_1 \times H_1 = 375\ \text{nm} \times 65\ \text{nm} \times 40\ \text{nm}$ and $g = 220$ nm, and dipole dimensions of $L_2 \times W_2 \times H_2 = 420\ \text{nm} \times 120\ \text{nm} \times 40\ \text{nm}$, the calculated transmittance, reflectance, and absorbance for full offset S and increasing vertical distance are shown in Fig. 6. The top row shows the calculations for $\gamma_D = 20$ THz, whereas the bottom row displays the idealized calculations with $\gamma_D = 1$ THz.

First, the case of high damping (top row) will be discussed. As is evident from the calculations, changing the geometry of the wires strongly alters the appearance of the spectra: these are not symmetric any more. For the dipole wire, absorbance is reduced; hence, the symmetric (blue shifted) mode of the structure, i.e., the one with a huge dipole moment, is attenuated in absorbance and appears more pronounced in reflectance. The opposite holds true for the antisymmetric mode, which exhibits more efficient coupling to the quadrupolar resonance due to its charge distribution [compare Fig. 3(b)]. Decreasing the width and height of the quadrupolar wires here leads to a strong increase in absorbance; hence, the mode shows up strongly pronounced in absorbance and rather weak in reflectance. The enhancement of absorbance shifts to significantly lower vertical spacings and the absorbance difference for $d_z = 30$ nm and $d_z = 90$ nm is less pronounced compared with that of the nondetuned situation. Still, the difference in modulation depth of the reflectance dip and the transmittance peak is observed, resulting in a subdipole-linewidth absorbance feature in the spectrum. The optimum vertical distance is found by comparing the absorbance peak for full offset ($S = 120$ nm) with that for zero offset. It occurs around $d_z = 90$ nm. To confirm these findings, the low gold damping case is also calculated for the detuned system. The spectra in the bottom row in Fig. 6 display the characteristic behavior of the system [compare Fig. 4(a)], even though the asymmetry of the spectral features is also observable. Hence, as already stated before, the main obstacle in the observation of the effect are the ohmic losses in the gold. But also for realistic damping values, it should be possible to observe it in the detuned structure.

To experimentally support the findings, a sample with several arrays of structures was fabricated using a two-step electron beam lithography process. The quadrupole and dipole sizes are approximately matched to the dimensions of the detuned structure. The spacer layer is $d_z \approx 100$ nm thick. The array size is 90 μm × 90 μm for each field. The offset S is varied from field to field in order to examine different coupling strengths. Due to limited overlay accuracy, the offsets of the fabricated structures have to be measured after fabrication. These are determined to be $S = 30$, 45, 60, and 150 nm. A

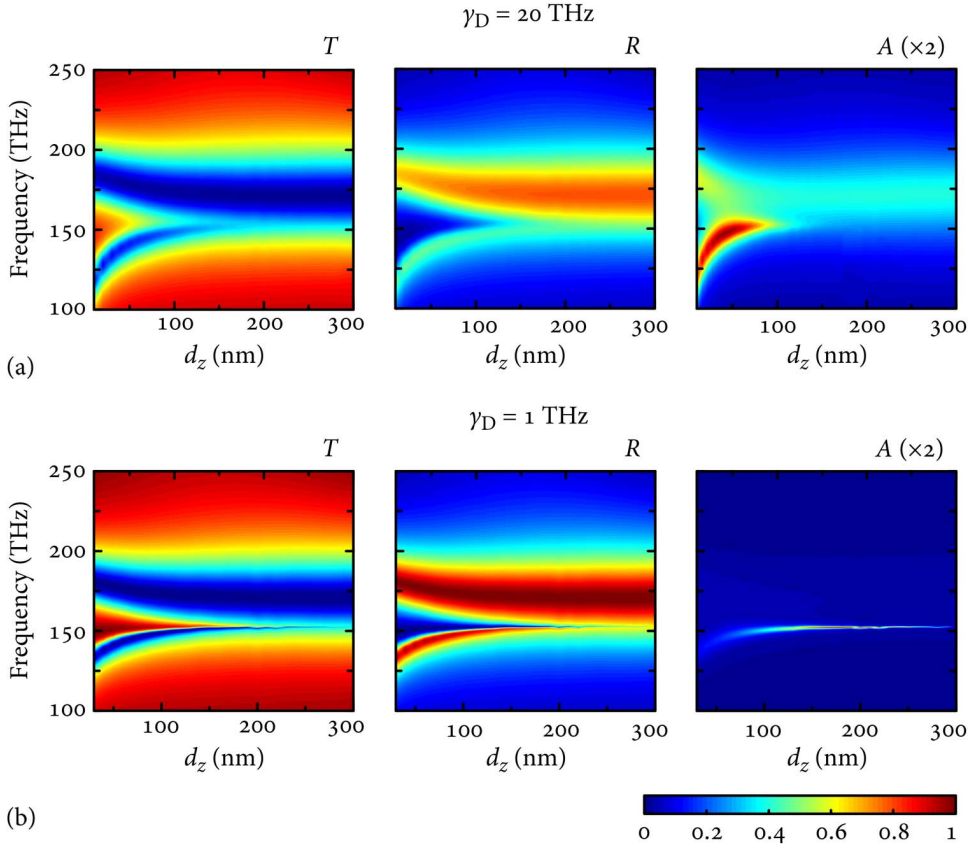

Fig. 6. (a), (b) Calculated transmittance, reflectance, and absorbance for increasing vertical distance d_z with a spectral detuning between the dipole and the quadrupole for a gold damping value of $\gamma_D = 20$ THz (top row) and 1 THz (bottom row). The spectral as well as scattering strength detuning lead to strongly asymmetric spectra, especially in the case of high damping. However, the EIA effect is still present, which is more pronouncedly observed in the bottom row.

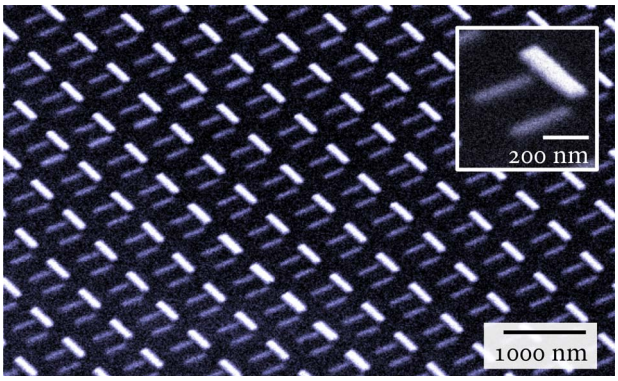

Fig. 7. SEM micrograph of the fabricated structure with maximum offset S. The inset displays one unit cell. Adapted with permission from Ref. [2]. Copyright: American Chemical Society (2012).

scanning electron micrograph of the fabricated structure with maximum offset is shown in Fig. 7. This image shows the large difference in wire sizes for the dipole and the quadrupole.

Reflectance and transmittance measurements for the different offsets are performed by Fourier transform infrared spectrometer (FTIR) measurement using a liquid nitrogen-cooled mercury cadmium telluride (MCT) detector. As absorbance will be calculated from the measurements of transmittance and reflectance, great care in alignment and during measurement has to be taken to achieve quantitatively comparable results in both measurements. The acquired spectra are shown in the left panel in Fig. 8(a). For comparison, calculations, based on realistic gold parameters, are displayed in the right panel.

The resulting absorbance spectra are displayed in Fig. 8(b). In these graphs, the double-peaked spectral shape is well pronounced. The small relative spectral shifts between the measurement and the simulation results are most likely due to deviations in the refractive index of the surrounding or slight changes in the actual nanoparticle morphology. For maximum offset S, the experimentally observed peak absorbance is 38%, compared with 28% in the uncoupled case, which corresponds to an enhancement of roughly 35%. In the calculations, this difference is even more pronounced, with a peak absorbance of 44% versus 20%, which corresponds to an increase by more than 100%. However, enhancement of the absolute value of absorbance is not the crucial point, as this can always be incorporated by introducing additional losses. In this case, the spectral width of the absorbance feature is smaller than the pure dipolar absorbance peak.

7. ANALYTICAL MODELING

A. Coupled Oscillator Model

Analogous to the straightforward description of EIT in terms of classical oscillators [15,34], the coupled oscillator model is also appropriate to describe EIA. The system shown in Fig. 9 is described by two coupled second-order differential equations

$$\ddot{x}_1(t) = \gamma_1 \dot{x}_1(t) + \omega_1^2 x_1(t) - \tilde{\kappa}' x_2(t) = f'_{\mathrm{ext}}(t) \tag{1}$$

$$\ddot{x}_2(t) = \gamma_2 \dot{x}_2(t) + \omega_2^2 x_2(t) - \tilde{\kappa}' x_1(t) = 0, \tag{2}$$

where the dipole and the quadrupole are represented by oscillator 1 and 2, respectively.

Only the dipole couples directly to the radiation field $f'_{\mathrm{ext}}(t)$. Crucial to the description of EIA is the use of a complex coupling coefficient $\tilde{\kappa}' = \kappa \exp i\varphi$, which is necessary to model the phase retardation effect. Using the harmonic ansatz $x_j(t) = a_j \exp(-i\omega t)$, $f'_{\mathrm{ext}}(t) = f' \exp(-i\omega t)$, and the approximation

$$\omega_j^2 - \omega^2 - i\omega\gamma_j \approx -2\omega_0\left(\omega - \omega_j + \frac{i\gamma_j}{2}\right) = -2\omega_0\Omega_j, \tag{3}$$

which is valid for $\omega \approx \omega_j \approx \omega_0$, the system can be simplified to

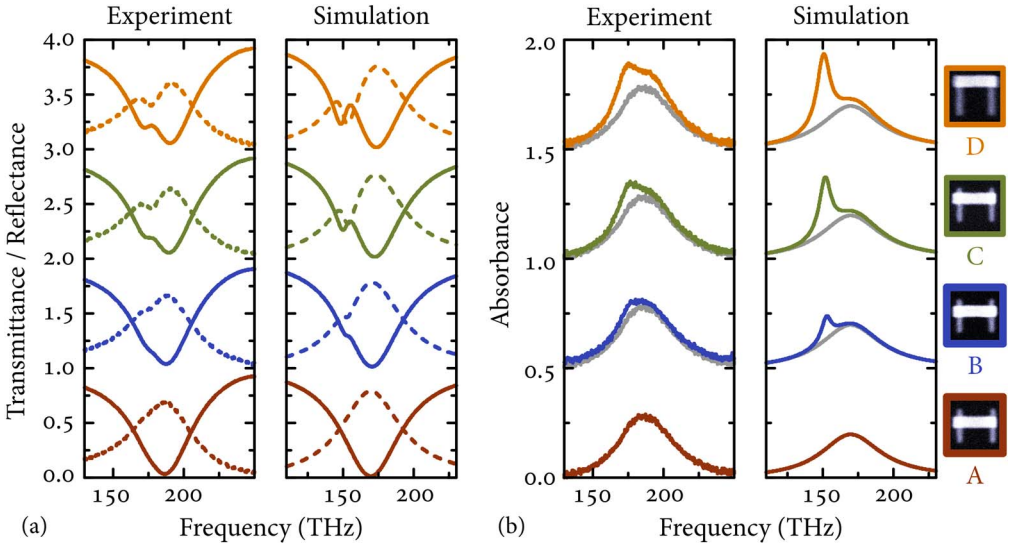

Fig. 8. (a) Measured (left) and calculated (right) transmittance spectra (solid curve) and reflectance spectra (dashed curve) for different offsets S. (b) Corresponding measured (left) and calculated (right) absorbance. In the simulations, a gold damping value of $\gamma_D = 20$ THz has been assumed. For increased offset S and therefore, increased coupling strength between the dipole and the quadrupole, a narrow absorbance dip originating from the excitation of the quadrupole appears. The minimum offset absorbance curve is shown in light gray in every graph for comparison. Simulated spectra are shown for offsets of 0, 40, 80, and 120 nm. Adapted with permission from Ref. [2]. Copyright: American Chemical Society (2012).

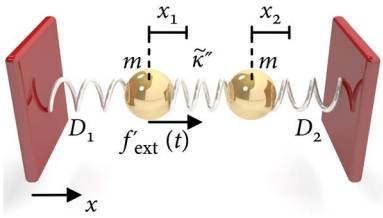

Fig. 9. Mechanical schematic of the coupled oscillator model for two oscillators with damping constants $\gamma_i = D_i/m$ and $\gamma_2 \ll \gamma_1$, coupled by $\tilde{\kappa}' = \tilde{\kappa}''/m$. Only the left oscillator is excited by the external force. For the implementation of EIA,$\tilde{\kappa}'$ has to be complex.

$$\begin{pmatrix} -2\omega_0\Omega_1 & -\tilde{\kappa}' \\ -\tilde{\kappa}' & -2\omega_0\Omega_2 \end{pmatrix}\begin{pmatrix} a_1 \\ a_2 \end{pmatrix} = \begin{pmatrix} f' \\ 0 \end{pmatrix}. \tag{4}$$

The solution is found by matrix inversion

$$\begin{pmatrix} a_1 \\ a_2 \end{pmatrix} = \frac{1}{\tilde{\kappa}'^2 - 4\omega_0^2\Omega_1\Omega_2}\begin{pmatrix} 2\omega_0\Omega_2 f' \\ -\tilde{\kappa}' f' \end{pmatrix}. \tag{5}$$

From this equation it is evident that the quadrupolar oscillator is excited only via the coupling to the dipole: the second oscillator amplitude a_2 is proportional to the external field multiplied by the coupling coefficient. The absorbance of the system is calculated as the dissipated power, which yields

$$A(\omega) = \Im\frac{2\omega_0\Omega_2 f'}{\tilde{\kappa}'^2 - 4\omega_0^2\Omega_1\Omega_2}. \tag{6}$$

Identifying $\Omega_1 = \omega - \omega_0 + i\gamma_1/2$ and $\Omega_2 = \omega - \omega_0 + \delta + i\gamma_2/2$ alongside normalized values $\tilde{\kappa} = (\tilde{\kappa}'/2\omega_0)$ and $f = (f'/2\omega_0)$, one arrives at

$$A(\omega) = \Im\frac{f\Omega_2}{\tilde{\kappa}^2 - \Omega_1\Omega_2}. \tag{7}$$

This equation is formally identical to those derived previously [1,3,5,15,32], except the complex coupling coefficient $\tilde{\kappa}$. The consequences of this complex coupling coefficient are discussed in Fig. 10. In this plot matrix, Eq. (7) is shown for different values of κ and φ. For $\varphi = 0$(first left column in Fig. 10), the spectra for a real coupling parameter are shown and therefore, the typical behavior of the EIT effect—a dip emerging on the broad dipolar absorbance feature—is observed. The uppermost row in Fig. 10 shows the spectra for almost vanishing coupling strength κ, where basically only the dipolar absorbance is present. For intermediate coupling strengths ($\kappa = 0.1$), a transformation from a small dip in the absorbance for $\varphi = 0$ to a small peak on top of the absorbance for $\varphi = \pi/2$ can be observed. However, this peak does not simply emerge out of the dip, but a rather complex behavior takes place. In the next row, $\kappa = 0.2$, this effect is more pronounced. The narrow peak emerges from the right maximum next to the dip, grows, and is most pronounced at exactly $\varphi = \pi/2$. At this φ value, it is furthermore symmetric around $\omega = \omega_0$.

For the parameter range from $\varphi = \pi/2$ to π, the spectra look identical but mirrored at the $\omega = \omega_0$ axis. This is a characteristic Fano behavior where the extreme case of a symmetric dip is realized for $\varphi = 0$ and the extreme case of a symmetric peak for $\varphi = \pi/2$.

An interesting situation occurs for large coupling strengths, as can be seen in the last row in Fig. 10: increasing the coupling strength beyond $\kappa > \sqrt{(\gamma_1\gamma_2/4)}$ leads to negative absorbance. Such a phenomenon of $A < 0$ has also been reported in atomic EIA spectra [12], a case, which corresponds to the presence of gain. Energetically, this does not constitute a

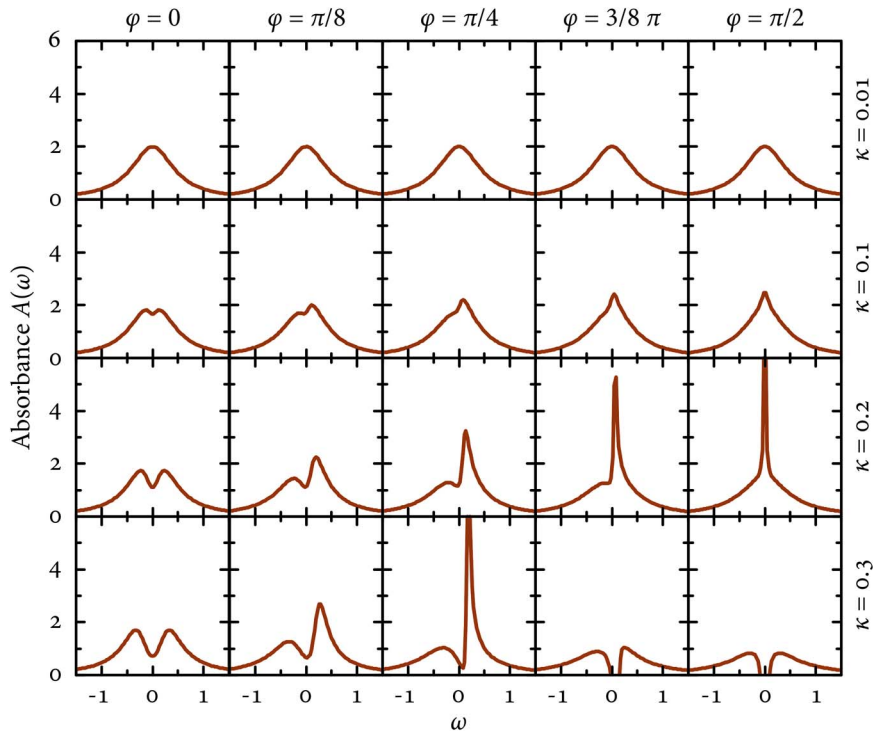

Fig. 10. Numerical evaluation of the analytical coupled oscillator formula, Eq. (7), with a complex coupling coefficient $\kappa \exp(i\varphi)$ for different combinations of κ and φ. All quantities are dimensionless. The other parameters are $\omega_0 = \delta = 0, f = 1, \gamma_1 = 1$, and $\gamma_2 = 0.2$.

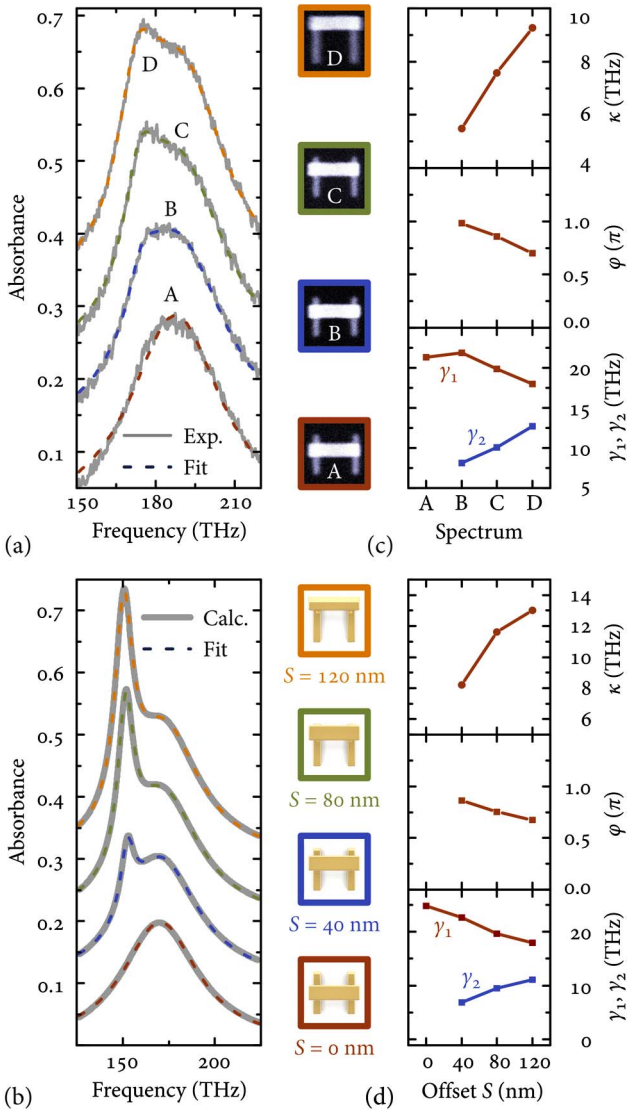

Fig. 11. (a), (b) Fit curves (dashed) of the coupled oscillator model with a complex coupling coefficient, Eq. (7), to the (a) experimental and (b) calculated absorbance spectra (solid graycurves). (c), (d) Retrieved fit parameters κ, φ, γ_1, and γ_2. Adapted with permission from Ref. [2]. Copyright: American Chemical Society (2012).

problem, as the atomic system is usually pumped by the coupling laser and therefore, gain should be possible. However, in a plasmonic system, this would violate energy conservation as no additional source of energy is present. In the coupled harmonic oscillator model, the situation of strong coupling with $\varphi = \pi/2$ corresponds to a strong force, which is exerted on the second particle in the wrong direction. This cannot occur in a real mechanical system. In the same manner, the classical radiatively coupled system has to ensure energy conservation and the case of $A < 0$ does not occur.

8. FITS TO EXPERIMENTAL AND CALCULATED SPECTRA

It is possible to fit Eq. (7) to the experimental as well as the calculated spectra. These are shown in Fig. 11. The parameters retrieved [42] from both fits are given in Table 1. Even though the fitting to the calculated spectra is more robust as the effect is more pronounced and can be observed unhampered by experimental difficulties such as noise and inhomogeneous broadening, there is reasonable qualitative agreement between both, the parameters extracted from the experimental and the calculated data. As expected, increasing the offset S yields an increase in the coupling parameter κ. For maximum offset, κ exceeds the dark mode linewidth in the calculated data; hence, the coupling from the dipole to the quadrupole is stronger than the dissipation processes in the metallic quadrupole wires. This is less pronounced in the experimental data; still, at least κ and γ_2 are of similar magnitude. The phase parameter φ also changes for increasing offset, starting from approximately π for the lowest offset and going to a final value of approximately 0.7π. This trend is quite well reproduced in both parameter sets. There is no straightforward explanation why φ ends up with an odd value instead of a more intuitive one such as a multiple of $\pi/2$ or π. However, one has to keep in mind that the system is more complex than suggested by the model, consisting of three oscillators, of which each possesses several loss channels, thus the maximum absorption does not necessarily occur for a phase, which is intuitively expected.

As an example, one would expect constructive interference for a phase delay in multiples of π—including 0. Still, the near-field-coupled EIT system obviously exhibits destructive interference instead, which indicates that the concept of plane wave interference is not directly applicable to this system of coupled oscillators in the intermediate coupling regime, in which near-field coupling effects still play a role.

Finally, the fitting parameters show that the quadrupolar linewidth is in fact smaller than the dipolar linewidth, which is already obvious from the spectra. However, it is of interest that the dipolar linewidth decreases consistently with increasing coupling strength, whereas the quadrupolar linewidth increases. In the naive coupled oscillator picture, these parameters should be constant as they are inherent oscillator properties and all coupling effects should be included within κ.

Table 1. Fit Parameters Obtained from Experiment and Simulation Using Eq. (7)[a]

	Theory				Experiment			
	A	B	C	D	0 nm	40 nm	80 nm	120 nm
κ	—	5.5	7.6	9.3	—	8.2	11.6	13.0
φ	—	1.0	0.9	0.7	—	0.9	0.8	0.7
γ_1	21	22	20	18	25	23	20	18
γ_2	—	8.2	10	13	—	6.8	9.2	11
f	6.1	7.0	7.2	8.0	4.9	5.3	6.1	6.6
ω_0	188	188	188	188	170	170	168	167
δ	—	13	13	13	—	16	12	10

[a]All parameters except φ are given in THz. φ is given in multiples of π.

This indicates that the coupled harmonic oscillator system is indeed a good model system, which captures the major features for the description of the effect, but the real system possesses a higher degree of complexity and therefore, our simple model does not capture all of the details.

9. ELECTRIC FIELD DISTRIBUTION IN THE EIA STRUCTURE

To further investigate the phase behavior of the oscillators, we perform electromagnetic field calculations for the structure. In the calculation, the detuned geometry with a vertical spacing of $d_z = 100$ nm and an offset of $S = 120$ nm is used. The field is calculated at a frequency of $f_q = 152$ THz, which corresponds to the quadrupole resonance frequency of the detuned structure.

As the EIA structure intrinsically depends on retardation effects, the field has to be evaluated in different planes perpendicular to the light propagation axis, as indicated in Fig. 12(a). Additionally, the field maxima at the dipole and the quadrupole do not necessarily occur at the same time due to retardation effects; hence, the time-dependent fields

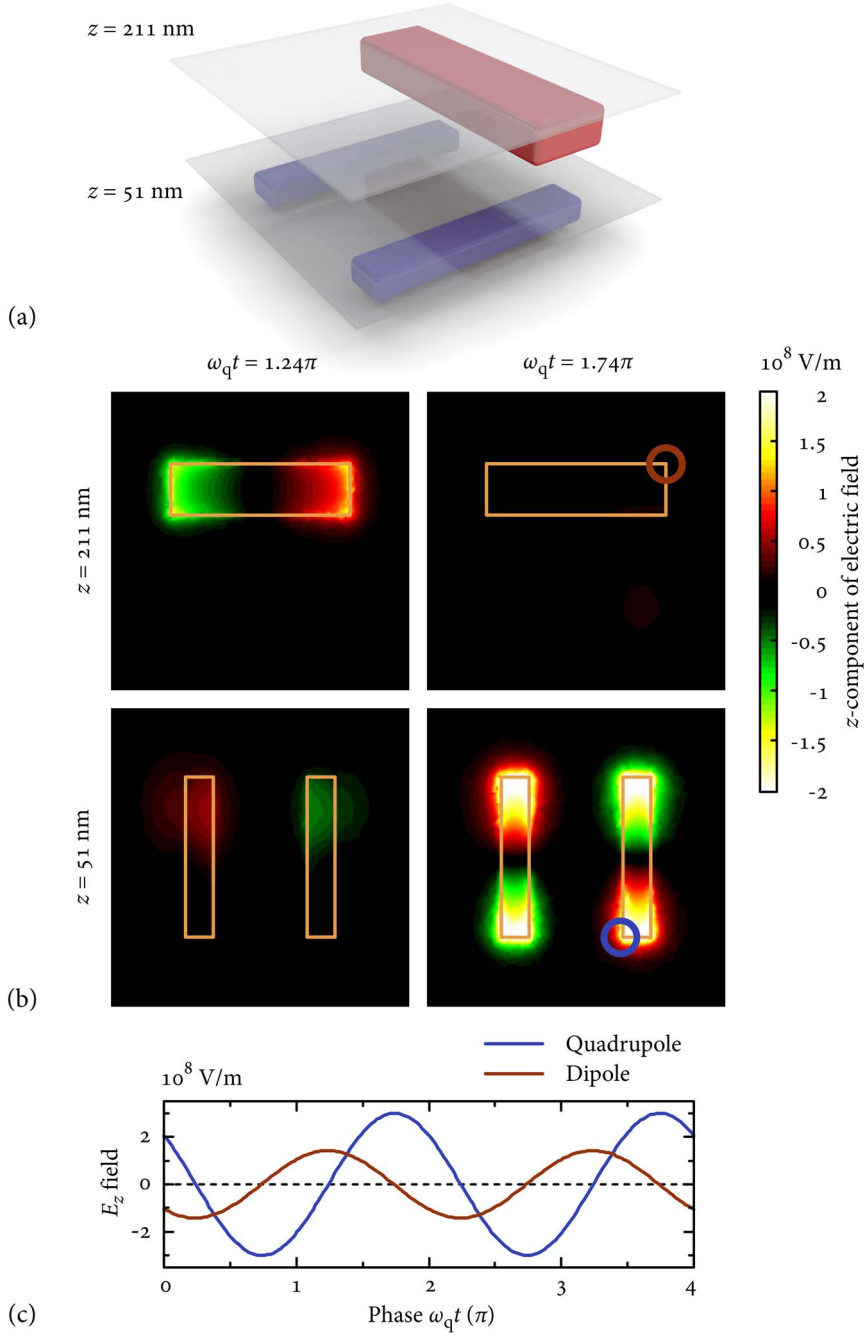

Fig. 12. (a) Schematic of the planes in which field calculations are shown. (b) Calculated z component of the electric field above the dipole (top row) and the quadrupole (bottom row) for $d_z = 100$ nm. Maximum field strength at the dipole and the quadrupole is observed at different times. z denotes the vertical position of the cross section. The dipole field is maximum for $\omega_q t = 1.24\pi$ (left column), whereas the quadrupole field is maximum for $\omega_q t = 1.74\pi$ (right column). (c) Calculated time evolution of the electric field strength at the dipole and the quadrupole tip [indicated by blue and red circle, respectively, in (b)]. Adapted with permission from Ref. [2]. Copyright: American Chemical Society (2012).

have to be considered. Thus, four different images of the z component of the calculated electric field are displayed in Fig. 12(b), for different planes, $z = 211$ and 51 nm, as well as phases of the light field $\omega_q t = 2\pi f_q t$. The latter are chosen by determining the maximum field strength at the dipole and the quadrupole. The field amplitude at the dipole reaches its maximum value for $\omega_q t = 1.24\pi$, whereas the field amplitude at the quadrupole is maximum for $\omega_q t = 1.74\pi$. For both maxima, the field at the respective other oscillator is very low, indicating an out-of-phase oscillation of the dipole and the quadrupole.

Comparing this field distribution to the ones obtained for the near-field-coupled EIT structure (see Fig. 3), the main difference between both cases can be observed: incase of EIT, the dipole excitation is canceled due to interference. At the quadrupole resonance frequency, no net plasmon oscillation is excited in the dipole wire, thus leading to high transmittance through the structure. By contrast, for EIA the resulting effect is an out-of-phase oscillation of the quadrupole and the dipole. This phase offset can be observed more clearly in Fig. 12(c) where the field intensity at two distinct points [indicated by circles in Fig. 12(b)] at the tip of the quadrupole (blue) and the dipole (red) is shown as a function of time. The quadrupole phase lags behind that of the dipole by $\pi/2$; therefore, the amplitude at one oscillator is zero for maximum amplitude at the respective other oscillator. This yields maximum energy dissipation and hence, a high absorbance in the structure.

This behavior of field maxima occurring at different times for different oscillators cannot be explained using only near-field coupling. As there are no phases in the pure near-field part, all coupled oscillators exhibit zero or π phase delay. Thus, the field distribution shows different amplitudes at different positions, but all the maxima are achieved at the same time in an oscillation cycle, which indeed is observed in the field plots of the EIT structure. Figure 12 shows that this is not the case any more in the EIA structure, and therefore, demonstrates the necessity of considering the phase in the latter.

10. CONCLUSION

In conclusion, this paper has given an overview of the plasmonic analog of electromagnetically induced transmission and absorption in a nanophotonic system, with major emphasis on the geometry consisting of a dipole cut-wire stacked on top of two cut-wires that form a plasmonic quadrupole. To tune the coupling and interference between the dipolar and the quadrupolar oscillator, an additional phase term was introduced. This additional phase was realized experimentally by increasing the vertical distance between the oscillators. In the case of constructive interference of the two excitations, we obtained enhanced absorption. This experimentally demonstrated an analog system to EIA for classical oscillators.

One interesting feature of this structure is that the vertical distance is in the intermediate regime and the coupling exhibits the characteristics of both, the near- as well as the far-field regime. Excitation of the quadrupole is still possible, but phase retardation due to enlarged spacing between the oscillators is already significant. Considering only radiative coupling would render the excitation of the quadrupolar oscillator impossible, while on the other hand, considering only near-field interaction would not allow retardation phases in the structure. This intermediate coupling regime offers new fascinating possibilities, such as phase control for coupling of plasmonic building blocks.

In the future, it will be intriguing to optimize our ansatz for plasmonic EIA by varying the geometry, coupling distance, detuning, as well as the metals. Obtaining sharp resonances would give enhanced nonlinear plasmonic interaction. In particular, a realization using superconductors that suppresses nonradiative contributions strongly would be highly exciting [43–45].

ACKNOWLEDGMENTS

The authors would like to thank Jürgen Kästel for insightful discussion. We gratefully acknowledge financial support by the Deutsche Forschungsgemeinschaft (SPP1391, FOR730, and GI 269/11-1), by the Bundesministerium für Bildung und Forschung (13N9048 and 13N10146), through the Advanced Grant COMPLEXPLAS from the European Research Council (ERC), by the Baden-Württemberg Stiftung, by the Ministerium für Wissenschaft, Forschung und Kunst Baden-Württemberg (Az: 7533-7-11.6-8) and by the German-Israeli Foundation. Publication of the manuscript has additionally been supported by publication funds of DFG.

REFERENCES AND NOTE

1. N. Liu, L. Langguth, T. Weiss, J. Kästel, M. Fleischhauer, T. Pfau, and H. Giessen, "Plasmonic analogue of electromagnetically induced transparency at the Drude damping limit," Nat. Mater. **8**, 758–762 (2009).
2. R. Taubert, M. Hentschel, J. Kästel, and H. Giessen, "Classical analog of electromagnetically induced absorption," Nano Lett. **12**, 1367–1371 (2012).
3. L. Verslegers, Z. Yu, Z. Ruan, P. Catrysse, and S. Fan, "From electromagnetically induced transparency to superscattering with a single structure: a coupled-mode theory for doubly resonant structures," Phys. Rev. Lett. **108**, 083903 (2012).
4. P. Tassin, L. Zhang, R. Zhao, A. Jain, T. Koschny, and C. M. Soukoulis, "Electromagnetically induced transparency and absorption in metamaterials: the radiating two-oscillator model and its experimental confirmation," Phys. Rev. Lett. **109**, 187401 (2012).
5. M. Fleischhauer, A. Imamoglu, and J. P. Marangos, "Electromagnetically induced transparency: optics in coherent media," Rev. Mod. Phys. **77**, 633–673 (2005).
6. S. E. Harris, J. E. Field, and A. Imamoglu, "Nonlinear optical processes using electromagnetically induced transparency," Phys. Rev. Lett. **64**, 1107–1110 (1990).
7. K. J. Boller, A. Imamoglu, and S. E. Harris, "Observation of electromagnetically induced transparency," Phys. Rev. Lett. **66**, 2593–2596 (1991).
8. U. Fano, "Effects of configuration interaction on intensities and phase shifts," Phys. Rev. **124**, 1866–1878 (1961).
9. A. M. Akulshin, S. Barreiro, and A. Lezama, "Electromagnetically induced absorption and transparency due to resonant two-field excitation of quasidegenerate levels in Rb vapor," Phys. Rev. A **57**, 2996–3002 (1998).
10. A. Lezama, S. Barreiro, and A. M. Akulshin, "Electromagnetically induced absorption," Phys. Rev. A **59**, 4732–4735 (1999).
11. A. V. Taichenachev, A. M. Tumaikin, and V. I. Yudin, "Electromagnetically induced absorption in a four-state system," Phys. Rev. A **61**, 011802(R) (1999).
12. A. Lipsich, S. Barreiro, A. M. Akulshin, and A. Lezama, "Absorption spectra of driven degenerate two-level atomic systems," Phys. Rev. A **61**, 053803 (2000).
13. S. E. Harris, "Electromagnetically induced transparency in an ideal plasma," Phys. Rev. Lett. **77**, 5357–5360 (1996).
14. G. Shvets and J. S. Wurtele, "Transparency of magnetized plasma at the cyclotron frequency," Phys. Rev. Lett. **89**, 115003 (2002).

15. C. L. G. Alzar, M. A. G. Martinez, and P. Nussenzveig, "Classical analog of electromagnetically induced transparency," Am. J. Phys. **70**, 37–41 (2002).
16. A. G. Litvak and M. D. Tokman, "Electromagnetically induced transparency in ensembles of classical oscillators," Phys. Rev. Lett. **88**, 095003 (2002).
17. K. Totsuka, N. Kobayashi, and M. Tomita, "Slow light in coupled-resonator-induced transparency," Phys. Rev. Lett. **98**, 213904 (2007).
18. Q. Xu, S. Sandhu, M. L. Povinelli, J. Shakya, S. Fan, and M. Lipson, "Experimental realization of an on-chip all-optical analogue to electromagnetically induced transparency," Phys. Rev. Lett. **96**, 123901 (2006).
19. A. Naweed, G. Farca, S. I. Shopova, and A. T. Rosenberger, "Induced transparency and absorption in coupled whispering-gallery microresonators," Phys. Rev. A **71**, 043804 (2005).
20. M. F. Yanik, W. Suh, Z. Wang, and S. Fan, "Stopping light in a waveguide with an all-optical analog of electromagnetically induced transparency," Phys. Rev. Lett. **93**, 233903 (2004).
21. D. D. Smith, H. Chang, K. A. Fuller, A. T. Rosenberger, and R. W. Boyd, "Coupled-resonator-induced transparency," Phys. Rev. A **69**, 063804 (2004).
22. L. Maleki, A. B. Matsko, A. A. Savchenkov, and V. S. Ilchenko, "Tunable delay line with interacting whispering-gallery-mode resonators," Opt. Lett. **29**, 626–628 (2004).
23. C. Wu, A. B. Khanikaev, and G. Shvets, "Broadband slow light metamaterial based on a double-continuum Fano resonance," Phys. Rev. Lett. **106**, 107403 (2011).
24. P. Tassin, L. Zhang, T. Koschny, E. N. Economou, and C. M. Soukoulis, "Low-loss metamaterials based on classical electromagnetically induced transparency," Phys. Rev. Lett. **102**, 053901 (2009).
25. N. Papasimakis, V. A. Fedotov, N. I. Zheludev, and S. L. Prosvirnin, "Metamaterial analog of electromagnetically induced transparency," Phys. Rev. Lett. **101**, 253903 (2008).
26. C. Wu, A. B. Khanikaev, R. Adato, N. Arju, A. A. Yanik, H. Altug, and G. Shvets, "Fano-resonant asymmetric metamaterials for ultrasensitive spectroscopy and identification of molecular monolayers," Nat. Mater. **11**, 69–75 (2011).
27. A. Artar, A. A. Yanik, and H. Altug, "Directional double Fano resonances in plasmonic hetero-oligomers," Nano Lett. **11**, 3694–3700 (2011).
28. A. Artar, A. A. Yanik, and H. Altug, "Multispectral plasmon induced transparency in coupled meta-atoms," Nano Lett. **11**, 1685–1689 (2011).
29. B. Luk'yanchuck, N. I. Zheludev, S. A. Maier, N. J. Halas, P. Nordlander, H. Giessen, and C. T. Chong, "The Fano resonance in plasmonic nanostructures and metamaterials," Nat. Mater. **9**, 707–715 (2010).
30. R. D. Kekatpure, E. S. Barnard, W. Cai, and M. L. Brongersma, "Phase-coupled plasmon-induced transparency," Phys. Rev. Lett. **104**, 243902 (2010).
31. N. Liu, T. Weiss, M. Mesch, L. Langguth, U. Eigenthaler, M. Hirscher, C. Sönnichsen, and H. Giessen, "Planar metamaterial analogue of electromagnetically induced transparency for plasmonic sensing," Nano Lett. **10**, 1103–1107 (2010).
32. S. Zhang, D. A. Genov, Y. Wang, M. Liu, and X. Zhang, "Plasmon-induced transparency in metamaterials," Phys. Rev. Lett. **101**, 047401 (2008).
33. B. Gallinet and O. J. F. Martin, "*Ab initio* theory of Fano resonances in plasmonic nanostructures and metamaterials," Phys. Rev. B **83**, 235427 (2011).
34. B. Gallinet and O. J. F. Martin, "Influence of electromagnetic interactions on the line shape of plasmonic Fano resonances," ACS Nano **5**, 8999–9008 (2011).
35. F. López-Tejeira, R. Paniagua-Domínguez, R. Rodríguez-Oliveros, and J. A. Sánchez-Gil, "Fano-like interference of plasmon resonances at a single rod-shaped nanoantenna," New J. Phys. **14**, 023035 (2012).
36. Z. Ruan and S. Fan, "Design of subwavelength superscattering nanospheres," Appl. Phys. Lett. **98**, 043101 (2011).
37. Z. Ruan and S. Fan, "Superscattering of light from subwavelength nanostructures," Phys. Rev. Lett. **105**, 013901 (2010).
38. T. J. Davis, D. E. Gómez, and K. C. Vernon, "Simple model for the hybridization of surface plasmon resonances in metallic nanoparticles," Nano Lett. **10**, 2618–2625 (2010).
39. N. Verellen, Y. Sonnefraud, H. Sobhani, F. Hao, V. V. Moshchalkov, P. Van Dorpe, P. Nordlander, and S. A. Maier, "Fano resonances in individual coherent plasmonic nanocavities," Nano Lett. **9**, 1663–1667 (2009).
40. S. H. Autler and C. H. Townes, "Stark effect in rapidly varying fields," Phys. Rev. **100**, 703–722 (1955).
41. B. Gallinet, T. Siegfried, H. Sigg, P. Nordlander, and O. J. F. Martin, "Plasmonic radiance: probing structure at the Angstrom scale with visible light," Nano Lett. **13**, 497–503 (2013).
42. In order to keep the fitting parameter space small for the experimental fits, the parameters ω_0 and δ are determined directly from the curve and kept fixed.
43. C. Kurter, P. Tassin, L. Zhang, T. Koschny, A. P. Zhuravel, A. V. Ustinov, S. M. Anlage, and C. M. Soukoulis, "Classical analogue of electromagnetically induced transparency with a metal–superconductor hybrid metamaterial," Phys. Rev. Lett. **107**, 043901 (2011).
44. S. M. Anlage, "The physics and applications of superconducting metamaterials," J. Opt. **13**, 024001 (2011).
45. A. Tsiatmas, A. R. Buckingham, V. A. Fedotov, S. Wang, Y. Chen, P. A. J. de Groot, and N. I. Zheludev, "Superconducting plasmonics and extraordinary transmission," Appl. Phys. Lett. **97**, 111106 (2010).